Fuel 407 (2026) 137329

Contents lists available at ScienceDirect

Fuel

journal homepage: www.elsevier.com/locate/fuel

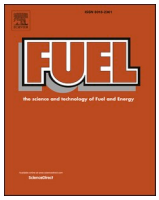

Full Length Article

Electrodeposited NiFe-succinate for the oxygen evolution reaction in anion exchange membrane water electrolysis

Andrea Zaffora [a], Valentina Maria Volanti [b], Leonardo Iannucci [b], Sabrina Grassini [b], Ilia Valov [c,d,e], Clara Saetta [f], Giovanni Di Liberto [f], Erminia Mosca [g], Irene Gatto [g], Vincenzo Baglio [g,*], Monica Santamaria [a,*]

[a] Dipartimento di Ingegneria, Università degli Studi di Palermo, Viale delle Scienze, Ed. 6, Palermo 90128, Italy
[b] Dipartimento di Scienza Applicata e Tecnologia, Politecnico di Torino, Corso Duca degli Abruzzi 24, Torino 10129, Italy
[c] Institute for Materials in Electrical Engineering and Information Technology (IWE2), RWTH Aachen University, Aachen D-52074, Germany
[d] Peter Grünberg Institute, FZ Jülich, Jülich D-52425, Germany
[e] Institute of Electrochemistry and Energy Systems, Bulgarian Academy of Sciences Akad. G. Bonchev 10, Sofia 1113, Bulgaria
[f] Dipartimento di Scienza dei Materiali, Università degli Studi di Milano Bicocca, Via Roberto Cozzi 55, Milano 20125, Italy
[g] Istituto di Tecnologie Avanzate per l'Energia "Nicola Giordano" (ITAE), Consiglio Nazionale delle Ricerche (CNR), Via Salita S. Lucia sopra Contesse 5, Messina 98126, Italy

ARTICLE INFO

Keywords:
$NiFe_2O_4$
Water electrolysis
Anion exchange membrane
Density functional theory
Oxygen evolution reaction

ABSTRACT

This study proposes Platinum Group Metal-free (PGM-free) electrocatalysts for the Oxygen Evolution Reaction (OER) to be used in Anion Exchange Membrane Water Electrolyzers (AEMWEs). NiFe-based electrodes were synthesized via an optimized electrodeposition process in the presence of succinic acid onto a low-cost 304 stainless steel (SS) mesh, resulting in an active and durable inorganic–organic complex. Morphological characterization confirmed the formation of high-surface-area electrodes, with a catalyst layer composed of Ni and Fe ions coordinated by organic carboxylic groups. X-ray Photoemission Spectroscopy (XPS) proved the formation of $NiFe_2O_4$ as the active species for OER, showing improved electrochemical performance compared to Ni-based and Fe-based electrodes. Notably, 240 mV and 306 mV were recorded as onset overpotential and overpotential at 10 mA cm^{-2}, respectively, with a low Tafel slope of approximately 50 mV dec^{-1}, using electrodes with total catalyst layer mass loading lower than 1 mg cm^{-2}. Density Functional Theory (DFT) calculations were performed to gain more insight into the OER mechanism on $NiFe_2O_4$ species, obtaining simulated polarization curves in very good agreement with experimental data. Finally, the best-performing electrode was tested in a single-cell AEMWE, achieving a maximum current density of 1.86 A cm^{-2} at 2.2 V and 60 °C, and demonstrating good stability after a 40-h chronoamperometric test conducted at 2 V.

1. Introduction

The growing demand for energy, along with the need to tame CO_2 emissions, calls for new and efficient solutions for storing and converting energy produced by renewable sources. Despite the increasing competitiveness of solar and wind power, their inherent intermittency and variability in output represent significant challenges. Therefore, developing new energy carriers is essential to ensure continuity and flexibility in energy supply.

In this scenario, green hydrogen emerges as a key resource; it is a clean fuel to generate energy via fuel cells and hydrogen combustion engines, and it is also a key element for low carbon emission industrial processes, like green ammonia production, and hard-to-abate sectors, such as steel production industry [1–4].

Water electrolysis is nowadays one of the most promising processes to obtain green hydrogen without carbon emission, if powered with renewable energy, obtaining hydrogen at the cathode and oxygen at the anode. Among different electrolysis technologies, alkaline water electrolysis (AWE) is the most common, because of the possibility to use cheaper platinum group metal (PGM)-free catalysts for electrodic reactions. In particular, electrode materials based on Ni, Co or stainless steels (SSs) are widely used in AWE. However, this technology suffers

* Corresponding authors.
E-mail addresses: vincenzo.baglio@itae.cnr.it (V. Baglio), monica.santamaria@unipa.it (M. Santamaria).

https://doi.org/10.1016/j.fuel.2025.137329
Received 26 August 2025; Received in revised form 10 October 2025; Accepted 24 October 2025
0016-2361/© 2025 The Author(s). Published by Elsevier Ltd. This is an open access article under the CC BY license (http://creativecommons.org/licenses/by/4.0/).

from high ohmic drops, which increase operating costs, and from the mixing of produced hydrogen and oxygen gases through the porous separator, hindering high gas purity and the possibility to get pressurized H_2 [4]. Recently, anion exchange membrane water electrolysis (AEMWE) is being studied because, potentially, it can combine pros of proton exchange membrane water electrolysis (PEMWE) and AWE, in terms of high purity hydrogen production, high efficiency, dynamic performance and the possibility to use cost-effective catalysts and stack components [5–7].

The efficiency of water electrolysis is limited by the Oxygen Evolution Reaction (OER), which requires very high overpotentials. Catalytic materials must operate under very harsh conditions, and an optimal bubble management is crucial. This stimulates the search for new catalysts and materials satisfying all these conditions, to reduce green hydrogen cost production and accelerate large scale production [8].

In this context, catalysts based on transition metals like Ni and Fe, have shown excellent catalytic activity towards OER in alkaline environment, offering an alternative to critical raw materials (CRMs)-based catalysts used in acidic environment, which are typically based on Ir [9], or in alkaline environment based on Pt [10].

Ni and Fe are often combined to optimize their structural and electronic properties, forming oxides, hydroxides and oxo-hydroxides, very active towards OER [11–13]. Alternatively, spinel-type $NiFe_2O_4$ has been also proposed as very high active species toward OER, due to the possibility of adjusting Ni/Fe content in the lattice, reaching optimized electrochemical performances [14–19].

Nevertheless, a crucial aspect in the development of these catalysts is their long-term stability in OER harsh operating conditions. The use of organic linkers can stabilize the materials and enhance their durability under alkaline conditions. Moreover, they can improve conductivity, morphology and porosity influencing the catalytic performance through functionalization effects, better distribution of the active sites and electronic and structural effects [20–23].

In this study, we developed a catalyst based on Ni and Fe, and an organic linker, derived from succinic acid, aimed at optimizing the electrocatalytic activity and the stability of the electrode for the OER. The catalyst was synthesized via electrodeposition onto a 304 stainless steel (SS) mesh substrate, which has been currently used as substrate for OER electrocatalyst [24–27]. This method enables the formation of uniform coatings [27] avoiding complex synthesis routes that typically involve high-temperature treatments or the usage of expensive and toxic precursors. Moreover, the process is easily scalable for industrial applications. [28–30]. Scanning electron microscopy (SEM) was used to study the catalysts' morphology, Infrared (FTIR) spectroscopy and X-ray photoelectron spectroscopy (XPS) were used to analyze their composition. Electrodes were tested in alkaline environment, assessing the effect of synthesis conditions on electrochemical performance toward OER. The short-term stability of the best-performing electrode was assessed through chronoamperometry tests both in a three-electrode cell and in a single-module AEM water electrolyzer. Quantum chemical simulations were performed to corroborate the experimental findings and provide an atomistic description of the nature of the active catalytic phase and on the way OER occurs on the catalyst.

2. Experimental

2.1. Materials

Succinic acid ($C_4H_6O_4$) has been purchased from J.B. Backer. $NiSO_4{\cdot}6H_2O$, $FeSO_4 \times 7\ H_2O$, H_2SO_4 and KOH were purchased from Sigma Aldrich.

2.2. Synthesis of NiFe electrodes

A stainless steel (SS) (AISI 304) mesh (provided by Molino Inox, mesh 91, wire diameter: 100 μm) was used as the substrate, undergoing a pretreatment in an ultrasonic bath containing acetone for a duration of 5 min followed by a second immersion in 0.5 M H_2SO_4 aqueous solution for 10 min. The electrodeposition bath was an aqueous solution containing 8.75 mM of succinic acid ($C_4H_6O_4$), 7.5 mM of $NiSO_4{\cdot}6H_2O$ and $FeSO_4{\cdot}7H_2O$, with a pH of 3.3 [27]. To make a comparison, electrodes containing only Ni and only Fe were synthesized using only the Ni-based or Fe-based salt during the electrodeposition process.

The electrodeposition process was conducted in a three-electrode cell setup, in which a Pt net was used as the counter electrode, an Ag/AgCl/3.5 M KCl electrode as the reference, and the SS mesh as the working electrode. An electrode potential of −1.4 V vs Ag/AgCl was applied to the pretreated SS electrodes for 15 or 30 min using a VERSASTAT 3 potentiostat at room temperature.

2.3. Morphological and compositional analysis

Images of the surface of the samples were acquired by using a FEI Quanta 200 FEG Scanning Electron Microscope, using EDX (X-ray Energy Dispersive system) to have information about the composition of the catalytic layers.

FTIR spectroscopy was performed at room temperature, with a Perkin-Elmer FT-IR/NIR Spectrum 400 spectrophotometer in a wavenumber range of 4000–400 cm^{-1}.

XPS spectra were recorded using a PHI 5000 VersaProbe II scanning XPS Microprobe (TM) with monochromatic Al-Kα radiation ($h\nu$ = 1486.6 eV) from an X-ray source operating at a 100 μm spot size, 25 W power, and 15 kV acceleration voltage. The high-resolution XPS spectra were collected using the hemispherical analyzer with a pass energy of 23.500 eV, an energy step size of 0.05000 eV, and a photoelectron take-off angle of 45° with respect to the surface. Peaks fitting was performed with MultiPak 9.9.0.8 (ULVAC-PHI, Inc), using Gauss-Lorentzian model and a Shirley type background.

Raman spectra were recorded through a Renishaw InVia Raman microscope, equipped with a 532 nm diode pulsed solid-state laser focused on the sample by means of a Leica DMLM microscope with a 100x long working distance magnification lens and a 1 μm spot.

2.4. Electrochemical measurements

All the electrochemical measurements were carried out using a conventional three-electrode electrochemical cell, using a PARSTAT 2263 potentiostat. The electrolyte used was a 1 M KOH aqueous solution, with a platinum mesh serving as the counter electrode, while a Hg/HgO/1 M NaOH electrode was employed as the reference electrode. All electrode potentials measured vs Hg/HgO were then referenced to the Reversible Hydrogen Electrode (RHE) for direct comparison with literature data, following the equation:

$$E_{RHE} = E_{Hg/HgO} + 0.098V + 0.059pH \quad (1)$$

The electrochemical active surface area (ECSA) was assessed by evaluating the double layer capacitance in an inert atmosphere to hinder oxygen reduction reaction, using a 0.1 M aqueous solution of ammonium biborate (ABE) (pH ≈ 9). To this aim, Electrochemical Impedance Spectroscopy (EIS) spectra at 0.1 V vs. RHE were recorded, over a frequency range of 0.1–10^5 Hz with an a.c. signal amplitude of 10 mV. The recorded spectra were then fitted using ZSimpWin software with an appropriate equivalent electrical circuit.

EIS spectra were also obtained at a potential of 1.52 V vs. RHE in a 1 M KOH electrolyte to evaluate electrocatalytic activity of all investigated samples. Potentiodynamic tests were carried out at a scan rate of 10 mV s^{-1}, starting from 0.92 V vs. RHE.

The stability of the electrocatalytic materials was assessed through chronopotentiometric measurements at 50 mA cm^{-2} for 100 h in 1 M KOH.

2.5. Electrode performances in AEM electrolyzer

NiFe samples were used as anodes for OER whilst cathodes were synthesized by preparing an ink mixing a commercial 40 wt% Platinum on Carbon (Pt/C, Alfa Aesar) and a 20 wt% of FAA3 ionomer (Fuma-Tech) in an ultrasonic bath for 30 min. Then, the ink was deposited by spray coating onto a Gas Diffusion Layer Sigracet 25-BC (SGL Carbon), with a final loading of 0.5 mg cm^{-2} [31]. As AEM, a FAA3-50® membrane (FumaTech), ~50 μm thick, was used.

Working area was set to 5 cm^2. AEM electrolyzer was characterized in a single-cell configuration in a temperature range between 30 °C and 60 °C, supplying a 1 M KOH solution to the anode compartment with a flow rate 5 ml min^{-1} controlled by a peristaltic pump (by Generalcontrol Srl). I–V curves were recorded at a scan rate of 5 mV s^{-1}. EIS spectra were recorded under potentiostatic control (at a cell voltage of 1.8 V and 2 V) in the frequency range from 100 mHz to 10 kHz by frequency sweeping in the single sine mode. The amplitude of the sinusoidal excitation signal was 10 mV r.m.s. A short chronoamperometric test was carried out at 2 V feeding a 1 M KOH aqueous solution for 40 h.

2.6. Computational analysis

Spin polarized Density Functional Theory (DFT) calculations were performed as implemented in the VASP package [32]. The Perdew-Burke-Ernzherof [33] parametrization was used to describe the exchange and correlation functional. Projector Augmented Wave pseudopotentials [34] were adopted to describe core electrons and valence electrons were expanded on a set of plane waves with a kinetic cutoff of 400 eV. Electronic structure optimizations were considered converged after achieving a threshold criterion of 10^{-5} eV between different steps. The PBE + U [35] approach was adopted to tame the self-interaction error of PBE. The U values have been taken from literature, $U_{Fe} = 3.3$ eV and $U_{Ni} = 5.5$ eV respectively [36]. The threshold for geometry optimizations was set 10^{-2} eV/Å. The Grimme's D3 scheme was used to account for dispersion forces. The Conjugate Gradient algorithm was adopted to search of minimum energy structures. The sampling of the reciprocal space was adapted to provide converged results. A working 5 × 5 × 5 grid was used for the bulk calculation.

OER was modeled by considering the four electrons reaction path passing from OH*, O*, OOH* intermediates. We have also considered the formation of other adducts observed on single-site catalysts [37]. The formation Gibbs free energy of OER intermediates was evaluated following the Computational Hydrogen Electrode (CHE) approach proposed by Norskov and co-workers in seminal works [38]. The Gibbs free energies were calculated from DFT energies, adding zero-point energy and entropic contributions. Zero-point energy was evaluated through the harmonic approximation. Entropy of solid-state species was neglected and that of gas-phase molecules was taken from international tables. This approximation leads to reasonable results, especially when the intent is not to extract absolute predictions, but to obtain the general trends.

3. Results and discussion

3.1. Compositional and morphological characterization

Electrocatalytic layers were synthesized by a cathodic electrodeposition process, starting from an aqueous solution containing a carboxylic acid (i.e. succinic acid) and Fe^{2+} and/or Ni^{2+} ions. Applying −1.4 V Ag/AgCl to the SS electrode for 15 min or 30 min, hydrogen evolution reaction (HER) occurs leading to a local OH^- concentration increase. This triggers the deprotonation of succinic acid producing succinate ions, which react with metal ions in solution inducing the crystallization of metallic succinate, where succinate ions work as ligand of Ni^{2+} and Fe^{2+} ions [27,39–42]. Usually, a pro-base can be used to locally increase the environment pH through the generation of a base that induces ligand deprotonation [39,43]. In our case, no pro-base was used as the local pH increases because of the HER occurring, consuming H^+ ions. Other than crystallization of metal succinate, deposition of metallic Ni and Fe cannot be excluded (see below) because of the high applied overpotential with respect to corresponding equilibrium potential at electrolyte pH, as well as the deposition of NiFe hydroxides [42,44].

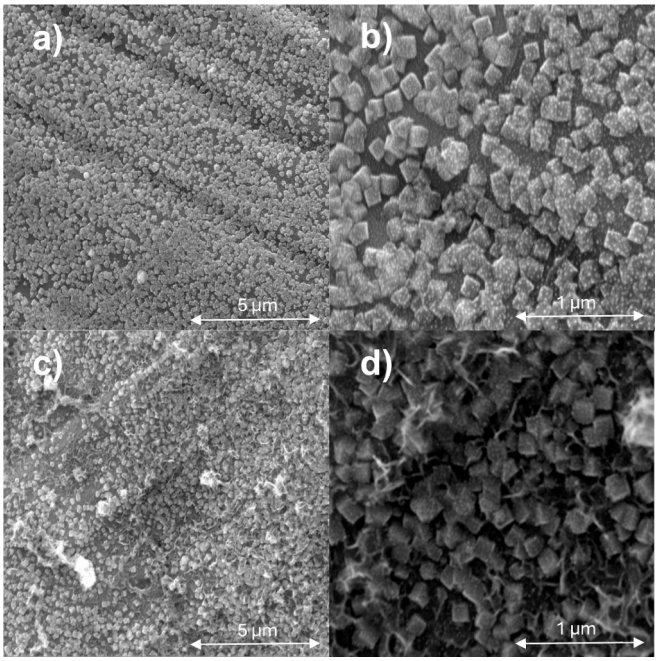

Fig. 1. SEM images of a), b) FeSuc-15 sample and c), d) FeSuc-30 sample. Magnification: a), c) 20000x and b), d) 80000x.

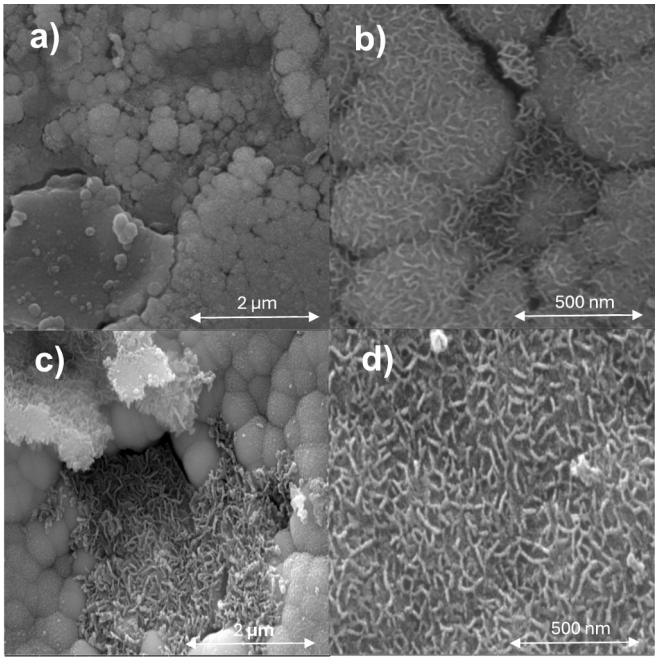

Fig. 2. SEM images of a), b) NiFeSuc-15 sample and c), d) NiFeSuc-30 sample. Magnification: a), c) 50000x and b), d) 200000x.

SEM images of SS mesh before and after electrodeposition are reported in Fig. S1a and b). At low magnification no differences can be detected. The morphology of electrocatalytic layer prepared through 15-min and 30-min electrodeposition processes (i.e. FeSuc-15, FeSuc-30,

Table 1
Atomic composition of 304 mesh sample and all the electrodeposited structures obtained by EDX.

Sample	C [at%]	O [at%]	Cr [at%]	Fe [at%]	Ni [at%]
304 mesh		10.86	17.97	63.45	7.72
FeSuc-15	9.58	7.91	16.29	60.62	5.59
FeSuc-30	7.04	8.83	16.23	61.33	5.3
NiFeSuc-15	12.71	22.73	7.53	34.56	20.99
NiFeSuc-30	21.3	25.91	3.92	23.42	24.38

NiFeSuc-15 and NiFeSuc-30), investigated at higher magnification, are reported in Figs. 1 and 2.

Firstly, it is worth noting that the mesh number of the 304 SS substrate may affect electrocatalyst loading and consequently OER performance. In this study, one mesh number was selected to guarantee comparability of the results. At lower magnification, the surface of FeSuc-15 sample (see Fig. 1a)) appears not uniform and not well covered, whilst a deposition time of 30 min results in a better coated sample (see Fig. 1c)). At higher magnification, both FeSuc-15 and FeSuc-30 samples exhibit a cubic-like morphology, with smaller particles observed on the surface of the microcubes (see Fig. 1b and d). At lower magnification, the overall surface of both NiFeSuc-15 and NiFeSuc-30 samples appear more uniform and better covered by the catalytic layer (see Fig. 2a and c), respectively) compared to the Fe-based samples. Moreover, a particle-rich structure is detected, with particles diameter on the order of hundreds of nm. A deposition time of 30 min results in larger particles, and a thicker coating formed by multilayers is also evident (see Fig. 2c)). Notably, each particle appears to be composed of a nanosheet array, which increases the available surface area at the nanometer scale. Similar nanosheet array morphologies have also been reported by other authors for NiFe-based organic–inorganic structures [45].

The composition of the samples deposited on SS mesh is detailed in Table 1. C and O originate from the coating, whereas Cr comes from the SS substrate. Ni and Fe signals come from both electrodeposited coating and the substrate. For NiFeSuc samples, the observed Fe content is lower than that measured in the SS bare sample and is consistent across all samples and areas, indicating that it primarily originates from the coating. Ni and C contents increase with deposition time, indicating the thickening of the coating from 15 to 30 min deposition.

FTIR analysis provides valuable insights into the molecular composition of the samples. FTIR spectra, related to NiFeSuc-15 and FeSuc-15 samples and pure succinic acid powder, are reported in Fig. 3.

Pure succinic acid spectrum reveals the presence of a peak around 1700 cm^{-1}, indicating the presence of C═O carboxylic group [46]. This peak shifts toward lower wavenumber for both FeSuc-15 and NiFeSuc-15 samples, indicating the coordination of succinic acid ligand with one or two metals, depending on the composition of the electrode. The broadband between around 3000 and 3500 cm^{-1} is due to the (O–H) stretching vibrations of water ligands, suggesting the presence of hydrogen bonds in the complex [46–50]. The vibrations of the carboxylate group, ν(C-OO^-), are observed in the spectrum related to pure succinic acid at around 1400 cm^{-1} (symmetric stretching) and 1300 cm^{-1} (asymmetric stretching) [46], and are also present in the spectra of both NiFeSuc-15 and FeSuc-15 samples. Notably, FTIR features remain unchanged with varying electrodeposition time.

Chemical state of NiFeSuc-15 surface sample was examined by XPS analysis, as well as those of FeSuc-15 and NiSuc-15 samples for comparison. As reported also from EDX analysis, surface of NiFeSuc-15 sample contains C, O, Ni and Fe, as can be seen from the survey scan XPS spectrum, reported in Fig. 4a). The presence of these elements further demonstrates the formation of a framework containing an organic part (i.e. the ligand) and a metallic part (i.e. Ni and Fe).

The main Ni $2p_{3/2}$ peak at 855.7 eV, along with the shoulder at 861.32 eV, can be attributed to Ni^{2+} species, such as those present in Ni$(OH)_2$ [45,51], while the peak at 852.15 eV can be related to the presence of metallic Ni, Ni^0. Fe $2p_{3/2}$ envelope at 711.45 eV, accompanied by a shoulder peak at 718.9 eV, can be attributed to Fe^{3+} species, such as those found in FeOOH, while the peak located at 706.21 eV corresponds to metallic Fe [52,53]. The presence of Ni^0 and Fe^0 can be explained by considering the possible electrodeposition of metallic species during the preparation of the electrocatalysts, as explained before. The C 1s XPS spectrum of the NiFeSuc sample is characterized by a peak located at 284.8 eV, that can be attributed to C–C and C–H group of adventitious carbon. Moreover, the peaks at 286.11 eV and 288.32 eV correspond respectively to the C from O–C═O and C–O from the organic ligand [54]. Analyzing O 1s spectra, a peak at 532.76 eV can be observed, corresponding to oxygen in the organic compound.. The peak at 531.26 eV can be associated with hydroxyl groups (–OH), in agreement with the presence of FeOOH and Ni$(OH)_2$. Another O 1s peak at lower binding energy (i.e. 529.43 eV) is attributed to the presence of oxygen in metallic oxides M−O. C, O, Ni and Fe present the same oxidation states in NiSuc-

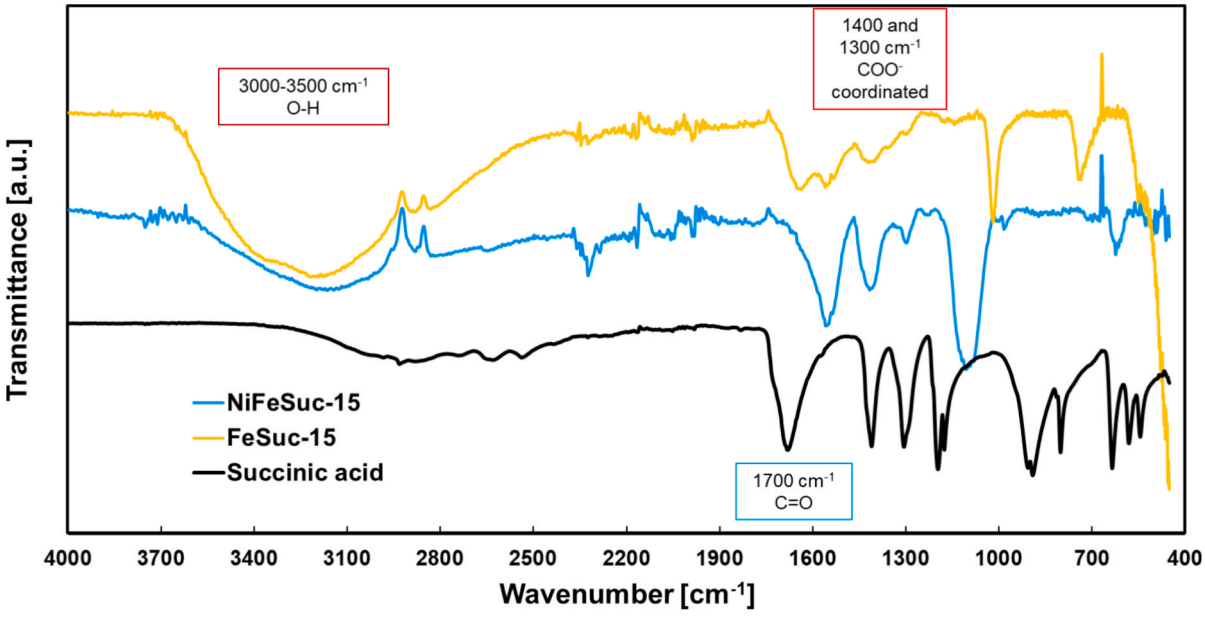

Fig. 3. FTIR spectrum related to NiFeSuc-15 sample, FeSuc-15 sample and succinic acid powder.

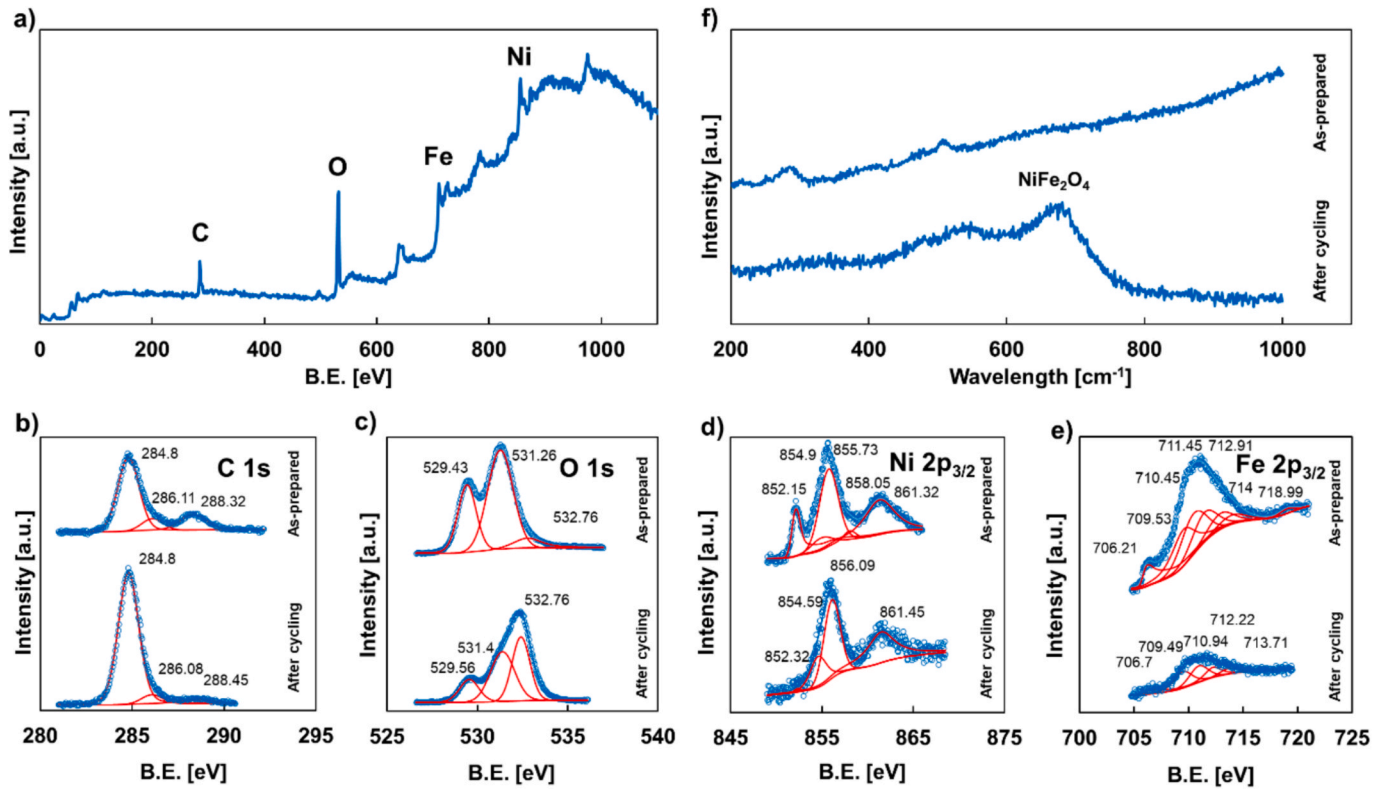

Fig. 4. XPS analysis of NiFeSuc-15 sample. a) survey scan spectrum, b) C 1s, c) O 1s, d) Ni $2p_{3/2}$, and e) Fe $2p_{3/2}$ spectra, for as-prepared sample and after electrochemical cycling. f) Raman spectrum for as-prepared NiFeSuc-15 sample and after electrochemical cycling.

15 (see Fig. S2a–c) and FeSuc-15 (see Fig. S2d–f) samples, which were studied for comparison with the NiFeSuc-15 sample, as confirmed by the corresponding XPS spectra [45,55,56].

The Electrochemical Active Surface Area (ECSA) is a crucial property for every electrode that should be used in electrocatalysis. In fact, electrochemical performances can be related to intrinsic electrocatalytic activity of materials involved in the reaction and to ECSA, as the latter directly reflects the effective active area of an electrode that participates in electrochemical reactions. A high ECSA indicates a large number of active sites on the electrode surface, which leads to more efficient electrocatalytic reactions.

To evaluate samples' ECSA, Electrochemical Impedance Spectroscopy (EIS) analyses were performed in an Ar-saturated 0.1 M ABE aqueous solution to determine the double layer capacitance values, C_{DL} [57]. These operating conditions ensure only non-faradaic processes take place, thus excluding possible contributions from faradaic current related to the oxygen reduction reaction (ORR). Nyquist plots for all recorded EIS spectra are presented in Fig. S3.

To extract meaningful information from EIS spectra, it is necessary to use an appropriate equivalent electrical circuit (EEC) to model the electrochemical behavior of the system at the specific working electrode potential values. The EEC employed to fit the impedance spectra for all the electrodes consists of a series combination of R_S (the solution resistance) and a parallel between R_{CT} (the charge transfer resistance) and Q_{DL}, which is used to model the non-ideal electrical double layer capacitance through a constant phase element (CPE) (see Fig. 5d, see below).

All fitting parameters are provided in Table S1. Fitting data reveal R_{CT} values, due to the absence of any faradaic reaction. C_{DL} values can be calculated from Q_{DL} using the given equation [57]

$$C_{DL} = Q_{DL}^{\frac{1}{n}} R_s^{\frac{1-n}{n}} \quad (2)$$

ECSA was evaluated through the estimation of a roughness factor, r, calculated using the following relationship [58]:

$$r = \frac{C_{DL}}{50 \mu F cm^{-2}} \quad (3)$$

referring to the C_{DL} value of a flat, mirror-polished AISI 304 coupon of 50 μF cm^{-2} [58]. r values are reported in Table 2 for all the investigated samples.

Bare 304 SS mesh has a roughness factor of about 1. Regarding NiFeSuc-15 and NiFeSuc-30 samples, r values of 8.7 and 16.9, respectively, were estimated whilst r values of 19.5 and 16.2 were estimated for FeSuc-15 and FeSuc-30 samples, respectively. These higher r values are correlated to peculiar electrodes' morphologies (see Figs. 1 and 2).

3.2. Electrochemical characterization

Electrochemical measurements have been carried out to assess the electrocatalytic activity of FeSuc and NiFeSuc samples. In particular, Linear Sweep Voltammetries (LSVs) and EIS spectra were recorded by using a standard three-electrode configuration in an alkaline aqueous 1 M KOH solution. LSVs are reported in Fig. 5a) for NiFeSuc and FeSuc samples, deposited for 15 and 30 min, considering a 95 % iR correction.

By looking at the polarization curves, it is evident that NiFe-based electrodes perform better than Fe electrodes, as already assessed in literature related to Ni and Fe-based electrodes for OER [59]. In all cases, the effect of deposition time on electrochemical performances is almost negligible. Interestingly, NiFeSuc-15 catalytic layer resulted to be very active despite having the lowest roughness factor, demonstrating that its enhanced activity originates from intrinsic electrocatalytic properties rather than from a larger active surface. In contrast, FeSuc samples had even higher r values, therefore indicating an even lower intrinsic electrocatalytic activity.

Onset overpotential value, η_{onset}, is different depending on the electrode used, being 240 mV and 320 mV for NiFeSuc and FeSuc

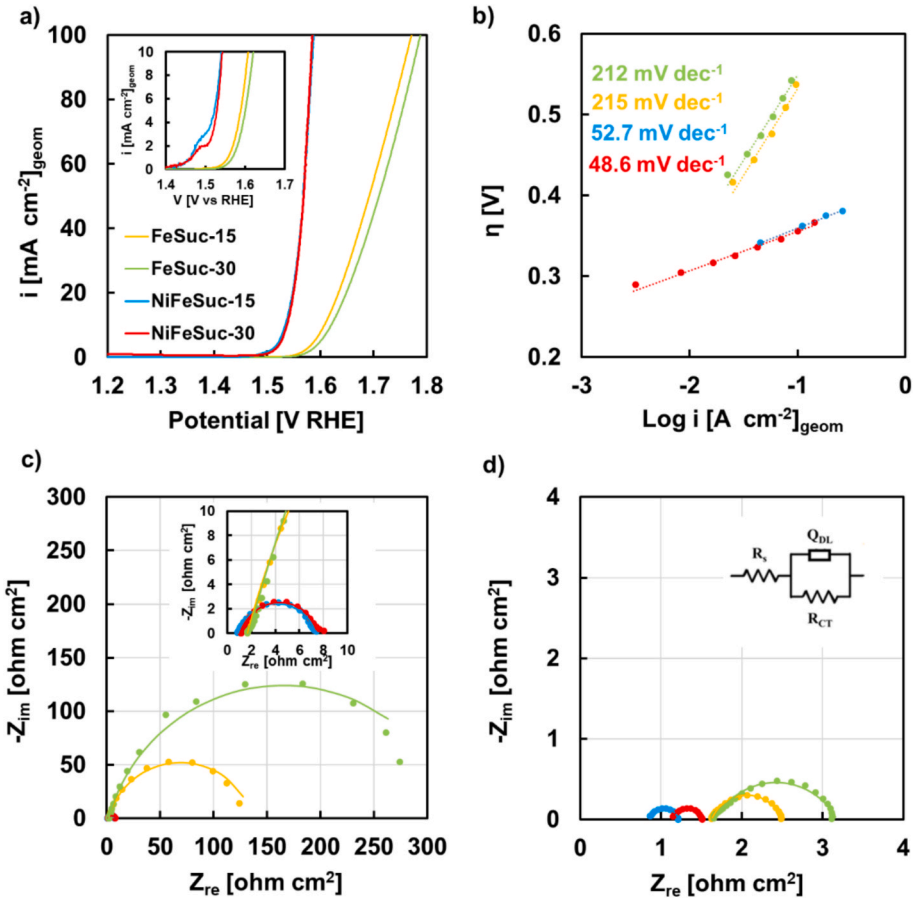

Fig. 5. a) Electrochemical performance of NiFeSuc and FeSuc electrodes in 1 M KOH aqueous solution at 25 °C (95 % iR correction). b) Corresponding Tafel plots; Nyquist plot of EIS spectra recorded at c) 1.52 V RHE and d) 1.67 V RHE for all the electrodes. Inset: equivalent electrical circuit used for fitting impedance data. Fitting data are those reported with continuous lines.

Table 2
Roughness factor, r, estimated for all the investigated electrodes.

	304 SS mesh	NiFeSuc-15	NiFeSuc-30	FeSuc-15	FeSuc-30
Roughness factor r	0.75	8.7	16.9	19.5	16.2

samples, respectively; therefore the presence of both metals in the electrocatalytic layer led to 80 mV reduction in onset electrode potential. A typical overpotential value used to assess electrocatalytic performances is the overpotential recorded at a fixed current density value of 10 mA cm^{-2}, η_{10}. The latter resulted to be 306 mV for NiFeSuc samples whilst it is comprised between 378 mV and 392 mV for FeSuc samples, the former comparable with some of the best OER electrochemical performances reported in literature with NiFe-based or SS-based electrodes [60]. Notably, these results have been reached with very low mass loading, being that latter lower than 1 mg cm^{-2} for NiFeSuc-15 electrode (see Fig. S9). Compared to other OER electrocatalysts, NiFeSuc samples performances are comparable to RuO_2, whose demonstrated η_{10} = 295 mV and a Tafel slope of 71 mV dec^{-1} [26], and outperform commercial IrO_2 deposited on carbon cloth in terms of η_{100} (i.e. 353 mV vs 415 mV for IrO_2) [61].

Better electrochemical performances exhibited by NiFeSuc-based electrodes are confirmed also by taking into account slope values of η vs log(*i*) plots (i.e. Tafel slopes), reported in Fig. 5b). In the case of NiFeSuc electrodes, Tafel slope values are close to 50 mV dec^{-1} whilst, in the case of FeSuc electrode, are close to 210 mV dec^{-1} indicating that

Table 3
Fitting parameters related to EIS spectra, recorded at 1.52 and 1.67 V RHE, reported in Fig. 5c) and 5d).

Sample	Potential [V RHE]	R_s [Ω cm^2]	R_{CT} [Ω cm^2]	Q_{DL} [S s^n cm^{-2}]	n	χ^2
FeSuc-15	1.52	1.71	134.6	1.8×10^{-3}	0.83	2×10^{-3}
	1.67	1.62	0.87	6.5×10^{-3}	0.76	6.5×10^{-5}
FeSuc-30	1.52	1.8	326.1	1.2×10^{-3}	0.82	5.8×10^{-3}
	1.67	1.7	1.5	8.5×10^{-3}	0.7	2.5×10^{-4}
NiFeSuc-15	1.52	0.89	6.46	1.04×10^{-2}	0.81	5.1×10^{-3}
	1.67	0.86	0.36	1.06×10^{-2}	0.82	5.03×10^{-5}
NiFeSuc-30	1.52	1.13	6.47	1.2×10^{-2}	0.84	4.1×10^{-4}
	1.67	1.13	0.38	1.5×10^{-2}	0.8	2.99×10^{-5}

lower electrochemical performances are probably due, not only to low intrinsic kinetic activity, but also to difficulties in mass transport. In fact, this high Tafel slope value can be related to non-kinetic effects, in particular to a harsh oxygen degassing at the electrode [62,63].

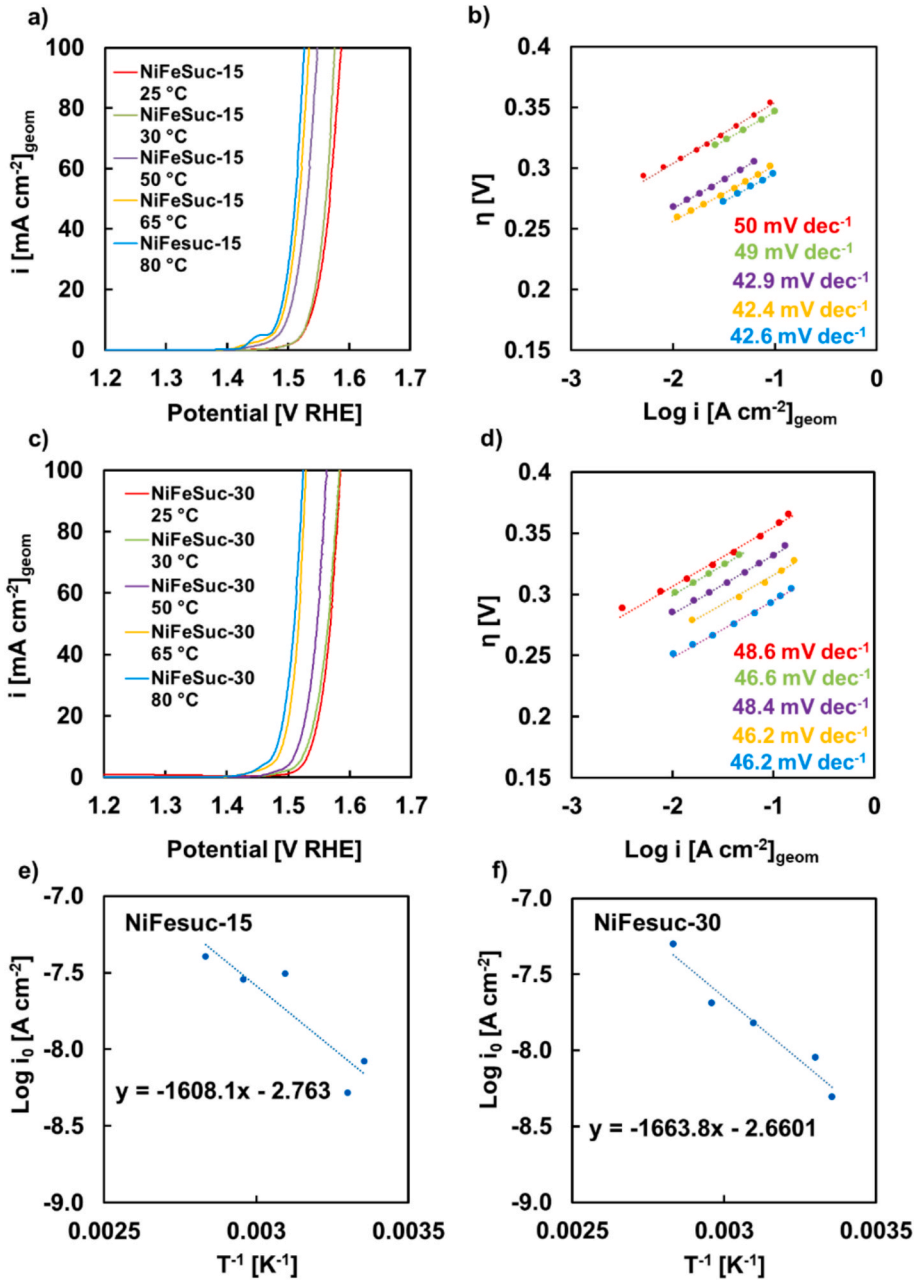

Fig. 6. Electrochemical performance of a) NiFeSuc-15 and c) NiFeSuc-30 electrodes in 1 M KOH aqueous solution at different bath temperatures (95 % iR correction). b) and d) Corresponding Tafel plots. Arrhenius plots, relating to exchange current density values, for e) NiFeSuc-15 and f) NiFeSuc-30 electrodes.

These results are further confirmed by EIS spectra recorded at 1.52 V RHE and 1.67 V RHE, reported in Fig. 5c and d) in Nyquist representation, respectively. To model the electrochemical behaviour, the equivalent electric circuit shown in the inset of Fig. 5d) has been used. Fitting parameters are reported in Table 3.

At 1.52 V RHE the reaction is still not activated for FeSuc sample as evident from the R_{CT} values, while it is well activated for NiFeSuc samples. These values further decrease at 1.67 V RHE and, in particular, it is noteworthy to mention that lower R_{CT} values are reported for NiFeSuc samples, in agreement with the results reported.

Important information can be derived from XPS analysis carried out on the electrodes after electrochemical characterization to assess OER performance (see Figs. 4b–e and S2a–f)). In the O 1s spectra, a reduction in the intensity of the peak at 531.26 eV, associated with hydroxyl groups, can be observed, while the peak at 529.5 eV, corresponding to oxides, shows an increase in intensity. After OER, changes in the intensity of the peaks related to C–O and O–C=O groups are also evident in the C 1s spectra. Additionally, the Fe^0 signal at 706 eV and the Ni^0 signal at 852.15 eV both decrease. A reduction in the Fe^{3+} signal is observed as well, along with a shift to 712.2–713.7 eV, suggesting the formation of a new species, i.e. $NiFe_2O_4$, with a spinel structure. This compound was reported as stable and very active toward OER in alkaline conditions [14,36]. The shift of the Ni peak from 861.32 eV to 861.45 eV in Ni spectra confirms the conversion to $NiFe_2O_4$, being also confirmed by the coexistence of different oxidation states of Ni and Fe [18,19]. This transformation can be attributed to the oxidation and subsequent rearrangement of Ni and Fe species, as indicated by the oxidation peak observed in the potentiodynamic curve for the NiFeSuc samples prior to the onset of OER (see Fig. 5a) [64–66]. These features are not unusual and have been widely documented in the literature for Ni–Fe based electrocatalysts [67–69]. They are generally assigned to the redox transitions of Ni(II) to Ni(III) (and in some cases to higher

oxidation states), and to possible oxidation of Fe species incorporated within the Ni matrix. Such transitions are commonly regarded as the electrochemical signature of the activation process leading to the formation of the catalytically active oxyhydroxide phase. In fact, the occurrence of these peaks prior to the OER onset is typically correlated with the generation of the actual active sites for oxygen evolution, although there is still debate as to whether Ni, Fe, or the synergistic interaction between the two elements is primarily responsible for the enhanced activity [70,71]. In the case of the monometallic samples, FeSuc and NiSuc, a decrease in the intensity of the peaks associated with metallic species is also observed, along with an increase in the peaks corresponding to oxidized species. However, based on electrochemical measurements, these oxidized forms demonstrate lower OER activity compared to the $NiFe_2O_4$ phase identified in the NiFeSuc sample. Notably, Raman spectrum recorded after electrochemical cycling of NiFeSuc-15 sample shows a characteristic band at ~ 700 cm^{-1}, typically associated with the presence of $NiFe_2O_4$, whilst the band a ~ 530 cm^{-1} can be ascribed to the presence of residual $Ni(OH)_2$ [72–74].

The impact of temperature on the electrochemical performance of NiFeSuc electrodes was assessed by performing tests with 1 M KOH as the electrolyte, recording LSVs at 25 °C, 30 °C, 50 °C, 65 °C, and 80 °C, the latter being the operating temperature of alkaline water electrolyzers at industrial level, as shown in Fig. 6.

As expected, increasing the operating temperature from 25 °C to 80 °C led to more visible oxidation peaks prior to OER onset and enhanced electrochemical performance, both due to improved reaction kinetics. As the temperature rises, the reaction rates increases (according to Arrhenius' law), resulting in a decrease in activation overpotential. A very slight decrease in the Tafel slope with increasing temperature is observed, indicating that the rate-determining step remains unchanged with varying operating temperature. The exchange current density, i_0, can be extracted from the Tafel plot by extrapolating the linear region to an overpotential of $\eta = 0$. For the evaluation of i_0, roughness factor, r, was taken into account; therefore, the exchange current density was estimated as $i_0 = i_{0,geom} \times r$. As expected, a linear relationship is observed between the logarithm of the exchange current density and the reciprocal of the operating temperature, in agreement with Arrhenius' law [75–77]:

$$\frac{\partial \ln(i_0)}{\partial \frac{1}{T}} = -\frac{E_a}{R} \tag{4}$$

Where E_a is the activation energy of the rate-determining step of the overall electrochemical reaction, R is the universal gas constant, T is the absolute temperature (in K). Therefore, from the slope of the Arrhenius plots (see Fig. 6e) and 6f)) activation energy can be calculated, obtaining 30.7 kJ mol^{-1} for NiFeSuc-15 electrode and 31.8 kJ mol^{-1} for NiFeSuc-30 electrode, being latter values of the same order of magnitude of other activation energy values reported in literature [75–77]. An increase in i_0 values can be also assessed by considering R_{CT} values, estimated as fitting parameters from EIS spectra (shown in Fig. S4a and b) recorded at 1.52 V RHE in 1 M KOH aqueous electrolyte at different operating temperatures, as reported in Tables S2 and S3. Since i_0 is inversely proportional to R_{CT} [76,77], this trend confirms the temperature dependence. Specifically, R_{CT} decreases from 6.5 Ω·cm^2 at 25 °C to 0.8 Ω·cm^2 at 80 °C for the NiFeSuc-15 electrode, indicating a significant enhancement in electrochemical kinetics. Same electrodes were also tested by changing KOH concentration in an aqueous electrolyte, between 1 M and 6 M (see Fig. S5a–d)), demonstrating that these electrodes can be also used in classical alkaline water electrolyzers, where KOH concentration between 4 M and 8 M are typically used [78,79].

To investigate the electrochemical stability of these catalysts, a chronopotentiometric test was carried at 50 mA cm^{-2}, in 1 M KOH, for 100 h, for the best electrode (i.e. NiFeSuc-15) in a flow-through configuration, emulating the behavior of the electrode in a real AEM electrolyzer.

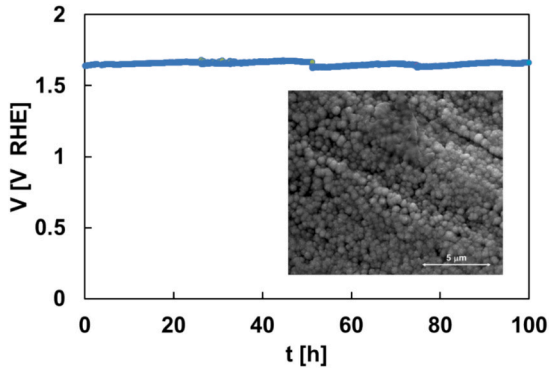

Fig. 7. Chronopotentiometry measurement for durability test of NiFeSuc-15 sample carried out at 50 mA cm^{-2} in 1 M KOH aqueous electrolyte for 100 h in flow through configuration. Inset: SEM image of the sample after chronopotentiometric test.

The overpotential for OER remains quite stable for (at least) 100 h, with a value of 420 mV ± 11 mV, demonstrating strong stability of NiFeSuc-15 electrode in harsh oxidizing conditions, as also shown by SEM image reported in Fig. 7, where it can be noted that sample surface still presents particle-rich structure after 100 h test.

3.3. Computational results

To model the OER reaction mechanism, we studied the $NiFe_2O_4$ species. Although $NiFe_2O_4$ is not the dominant phase in the electrodeposited samples, it is recognized as one of the most active phases for OER. Therefore, $NiFe_2O_4$ was used as a model for theoretical calculations.

We started with the experimental cubic bulk crystal structure. The calculated lattice vectors a = 5.822 Å, b = 5.826 Å and c = 8.278 Å compare well with experimental data, $a = b$ = 5.88 Å and c = 8.26 Å. Low-index (0 0 1) and (1 1 0) surfaces were modelled from the bulk structure (see Fig. 8). The selection of these planes was determined as they are low-index surfaces within the spinel structure and show small surface energies, which renders them the most probable candidates to be exposed under the prevailing experimental conditions. The slabs were generated by cleaving the fully relaxed bulk cell along these crystallographic planes and creating models without artificial surface dipoles. Table S4 reports the lattice parameters and thickness of the $NiFe_2O_4$ models [80]. Experimentally, the (0 0 1) face is the dominant one in $NiFe_2O_4$. The (0 0 1) surface one shows two different terminations, FeO or NiO. The (0 0 1) surface was modelled by considering a 2 × 2 expansion of the primitive cell, a = 11.755 Å, b = 11.762 Å and γ = 90°. The working simulation cell of (1 1 0) surface was constructed by cutting the bulk cell along the (1 1 0) direction with lattice parameters equal to a = 8.260 Å, b = 8.315 Å and γ = 90°. In all cases the atomic coordinates were fully relaxed.

The calculated surface energy of the three surface models investigated in this work is 1.58 J/m^2, 1.72 J/m^2 and 1.98 J/m^2, for FeO-(001), (110) and NiO-(001) respectively. This indicates that FeO-(001) is more stable than NiO-(001). The (110) surface shows an intermediate stability.

We started the analysis from the most stable surface model, FeO-terminated (001) surface [36,80–82]. The structure of the catalyst is reported in Fig. 9a), where surface Fe atoms, "Fe_1", are available for OER, and Fig. 9b) shows the calculated Gibbs free diagram at V = 1.58 V vs *RHE*.

As it is possible to note from the Gibbs free energy diagram (see Fig. 9b), at the working potential of 1.58 V RHE, i.e. the potential required to have a current density of almost 80 mA cm^{-2} at 25 °C indicating that the reaction is already well activated (see Fig. 5a)), the reaction should pass by the formation of OH*, followed by an oxidation

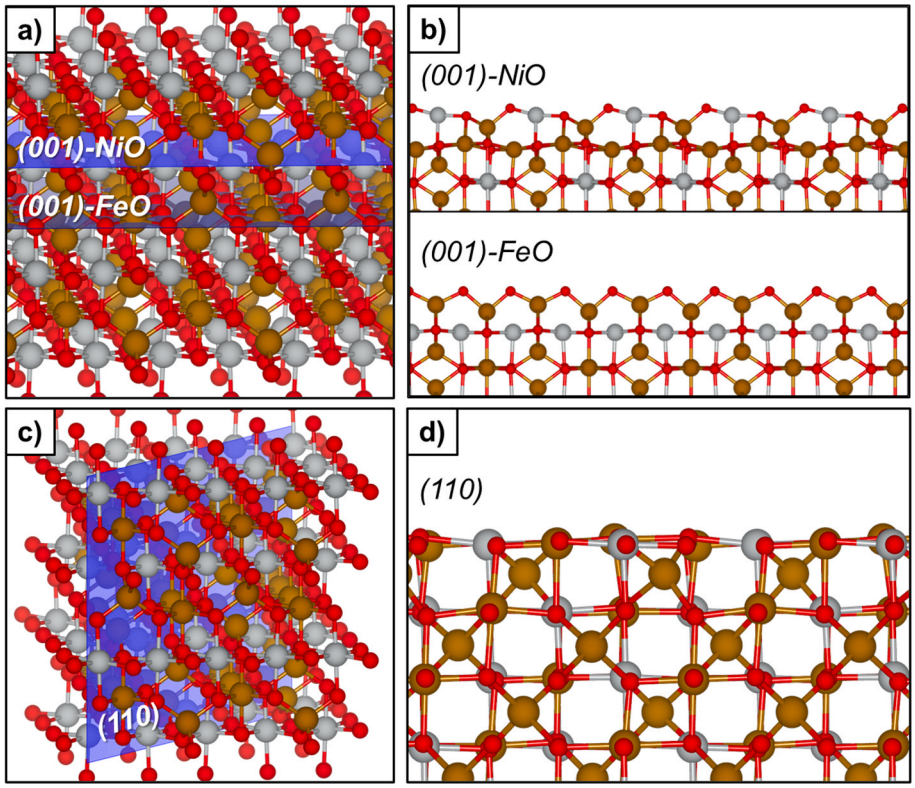

Fig. 8. a) Bulk structure with (001) planes cutting along the two possible terminations, b) two (001) surfaces with different terminations, c) bulk structure with (110) plane cutting to generate the surface in Fig. 1(d).

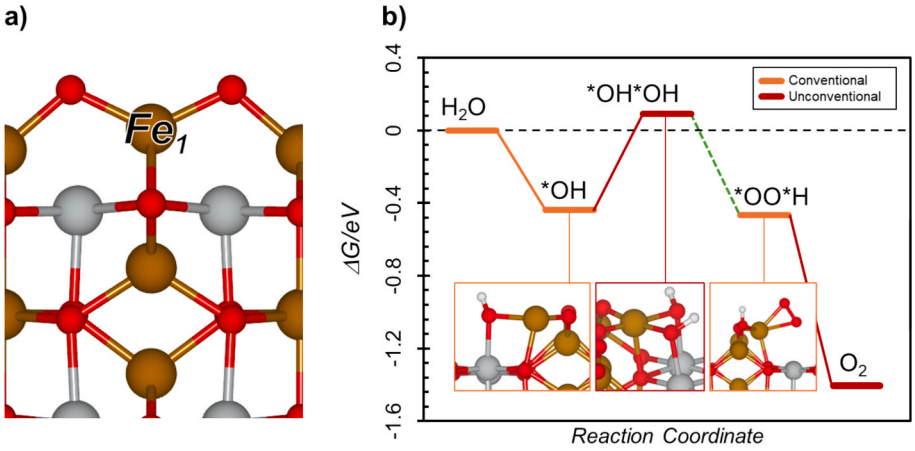

Fig. 9. a) Active site for OER on nichel ferrite (001) surface, FeO termination. b) Free energy diagram of the OER on the (001) FeO termination. Conventional intermediates are reported in orange, unconventional ones (red). (For interpretation of the references to colour in this figure legend, the reader is referred to the web version of this article.)

step leading to OH*OH* [37,83]. This intermediate is more stable than O*. Then, a proton-electron couple is released, leading to *OO*H before the release of molecular oxygen. The largest thermodynamic barrier is equal to 0.53 eV and corresponds to the reaction step from OH* to OH*OH*. This value corresponds to a thermodynamic barrier of 51 kJ mol^{-1}; considering the number of inherent approximations in the model and the complexity of the system and catalytic process, the calculated value can be considered in reasonable agreement with the estimated value using Eq. (4) starting from experimental data measured at several operating temperatures. All the other reaction steps proceed with a decrease in energy. Looking at the intermediate geometry, we see that oxygen prefers to assume a bridge position in every intermediate, coordinating both Fe and Ni atoms. This can be a very important insight into the electrocatalytic cooperation between the metals. Furthermore, in some cases Fe reaches a pseudo-square planar coordination on the top layer, displacing itself with respect to the lattice position. The bonds between Fe and O measure around 1.69–2.03 Å while between Ni and O are in the range of 2.01–2.07 Å, assuming almost the reticular position (where $d_{Fe\text{-}O}$ = 1.93–2.01 Å and $d_{Ni\text{-}O}$ = 2.06–2.18 Å). The mechanism occurring on this surface matches with the experimental data, therefore we expect it to be the most favorable to happen.

We also considered the OER on the NiO-terminated (001) surface. The calculated Gibbs free energy profile is reported in Fig. S7. Overall, the process is associated with much larger reaction barriers, indicating a

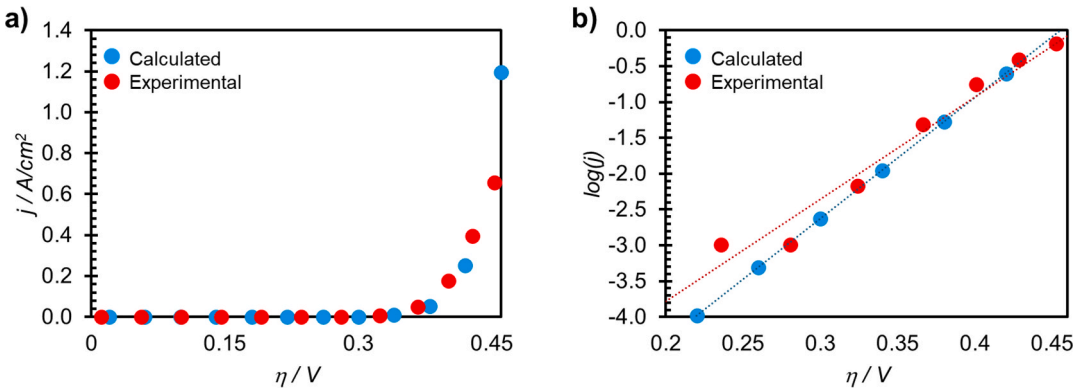

Fig. 10. a) Calculated and experimental polarization curves related to OER on NiFeSuc-15 electrode and b) corresponding Tafel plot. Red dots: experimental data, blue dots: calculated values based on eq.(5). (For interpretation of the references to colour in this figure legend, the reader is referred to the web version of this article.)

lower reactivity of this system. On the other hand, we also simulated OER on the (110) surface. In this case, the system is too reactive, forming too stable intermediates. The calculated Gibbs free energy profile is reported in Fig. S8.

We started from the calculated Gibbs free energy profile and simulated the polarization curve to check for the actual agreement between the simulated catalytic model and reaction profile with the experimental measurements.

We used the generalized Butler-Volmer model [84]:

$$j(n) = f(G^{\#}_{rds}, \beta_{RDS}) \approx \frac{4k_B T}{h} e\,\Gamma_{act} e^{-\frac{G^{\#}_{RDS}}{k_B T}} e^{\frac{\beta_{RDS} e}{k_B T}\eta} \quad (5)$$

where j is the current density, k_B is the Boltzmann constant, T is the temperature, set to 25 °C, h is the Planck's constant, e is the charge of the electron, $G^{\#}_{RDS}$ is the barrier of the rate determining step (from OH* to OH*OH*). We used a value of $\Gamma = 2 \times 10^{16}$ sites/cm^2. β_{RDS} is the number of electrochemical step before the resting state (in this case 0) and η is the overpotential.

In Fig. 10a) the comparison between experimental and calculated curves is reported and Fig. 10b) shows the corresponding Tafel plot for both graphs. The simulated curve reproduces the measured one, indicating the reliability of the simulated catalytic model and reaction profile.

As observed, the simulated polarization curve closely matches the experimental data, confirming the reliability of the electrocatalytic model and the proposed reaction pathway, supporting the relevance of $NiFe_2O_4$ as the key active species in the catalyst. This agreement provides a solid explanation of how the NiFeSuc electrode operates effectively under the investigated conditions.

3.4. AEMWE testing

To further test the electrodeposited electrode, we scaled up the electrodeposition process preparing NiFeSuc-15 electrode to be also employed as the anode in a single-cell electrolyzer module, which consisted of Ni plates featuring a single-serpentine flow field with an active area of 5 cm^2, sandwiched between external gold current collectors. The membrane electrode assembly (MEA) consisted of a NiFeSuc-15 anodic electrode, an FAA3-50® membrane serving as the anion exchange membrane (AEM), and a Pt/C electrocatalyst deposited onto a carbonaceous backing layer as the cathode. The electrolysis cell was characterized using linear sweep voltammetry (LSV), with 1 M KOH aqueous solution fed to the anode. Measurements were conducted at various operating temperatures ranging from 30 °C to 60 °C. The LSV curves recorded at these different temperatures are shown in Fig. 11a).

As widely reported in the literature, the electrochemical performance of the AEM electrolyzer improves with increasing operating temperature [85–90]. This enhancement is primarily attributed to a decrease in activation loss contribution due to the enhancement in kinetics of HER and OER at the electrodes as well as to a higher ionic conductivity of AEM [85]. Specifically, raising the operating temperature from 30 °C to 60 °C resulted in a slight decrease in onset cell voltage and an increase in maximum current density at 2.2 V, from 1.0 A cm^{-2} at 30 °C to 1.86 A cm^{-2} at 60 °C. This temperature-dependent behavior is further supported by EIS measurements, as shown in Fig. 11b), where

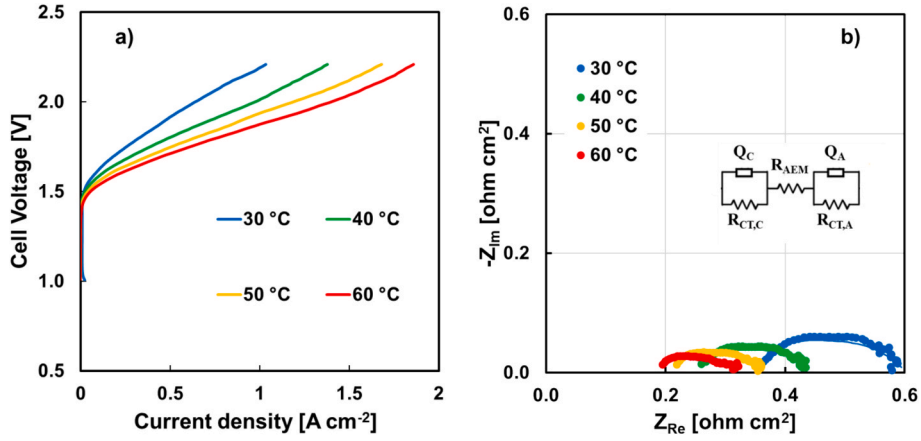

Fig. 11. a) LSVs recorded at different temperatures employing NiFeSuc-15 electrode as anode in an AEM electrolyzer and b) EIS spectra in Nyquist representation recorded at 1.8 V using the same experimental setup. Fitting: continuous lines. Inset: EEC used to fit the data.

Table 4
Fitting parameters related to EIS spectra, recorded at 1.8 V at different operating temperatures, reported in Fig. 11b).

T	R_{AEM} [Ω cm^2]	$R_{CT,C}$ [Ω cm^2]	Q_C [S s^n cm^{-2}]	n	$R_{CT,A}$ [Ω cm^2]	Q_A [S s^n cm^{-2}]	n
30 °C	0.35	0.06	7×10^{-3}	0.86	0.19	0.14	0.56
40 °C	0.25	0.05	9×10^{-3}	0.83	0.14	0.19	0.56
50 °C	0.20	0.02	7×10^{-3}	0.97	0.15	0.19	0.50
60 °C	0.18	–	–	–	0.068	0.04	0.67

EIS spectra recorded at 1.8 V between 30 °C and 60 °C are reported. In this context, the electrochemical response of the whole electrolyzer can be modelled using the EEC reported in the inset of Fig. 11b), i.e. by considering two parallel RQ elements, representing the cathode and anode, in series with a resistance representing the series resistance [91,92], where the highest contribution is related to ionic resistance of the AEM, denoted as R_{AEM}. Fitting parameters are reported in Table 4.

It can be observed that increasing the operating temperature leads to a decrease in the series resistance, due to the enhanced OH^- conductivity of the AEM. Specifically, the resistance drops from 0.35 Ω·cm^2 at 30 °C to 0.18 Ω·cm^2 at 60 °C. R_{AEM} values derived from EIS measurements fit well with the resistance values estimated by considering ohmic drop region in Fig. 11a), which vary between 0.52 Ω·cm^2 at 30 °C and 0.32 Ω·cm^2 at 60 °C. Additionally, a reduction in the overall cell impedance is also evident with rising temperature, which can be directly attributed to improved electrode kinetics for both the HER and OER. This can be directly assessed by looking at R_{CT} values of both electrodic reactions reported in Table 4, which decrease by increasing T from 30 °C to 60 °C. Notably, $R_{CT,C}$ values are, in any operating condition, one order of magnitude lower with respect to $R_{CT,A}$, which is expected by using Pt/C electrocatalyst at cathode. Moreover, in the case of T = 60 °C, cathode can be excluded from equivalent circuit since HER charge transfer resistance is too low to be detected. The possible presence in the impedance spectrum of more than one time constant can be related to other loss mechanisms, such as ionic transport in the catalyst layer [93].

A short-term (~ 40 h) durability test was carried out under potentiostatic mode at 2 V to evaluate, at least, the short-term stability of the electrochemical performance of AEMWE using NiFeSuc electrode at the anode side. The resulting chronoamperometric curve is reported in Fig. 12a).

As observed, the current density slightly decreased over time, especially during the first few hours of the test. However, toward the end of the test, the decrease became less pronounced. The current density peak at ~ 20 h can be ascribed to the test restarting after the 1 M KOH solution was replenished. This behaviour is consistent with past studies, where a drop in current density value was observed and ascribed to possible various mechanisms occurring during cell operation, e.g. membrane degradation or poisoning due to formation of carbonates in presence of CO_2, catalysts deactivation or electrodes issues (e.g. challenges with bubbles removal from electrode surface) [86,89]. To gain more insight into possible degradation mechanisms, LSV and EIS experiments were performed before the chronoamperometric test (BoT, Beginning of Test) and after the chronoamperometric test (EoT, End of Test) at 60 °C, as shown in Fig. 12b). As expected, the LSV results showed a decrease in cell performance at EoT, with an increase in ohmic drop, resulting in a current density of 1.05 A cm^{-2} at 2 V. This can also be observed by comparing the impedance spectra (see inset of Fig. 12b) recorded at 2 V under both BoT and EoT conditions, where an increase in R_{AEM} can be noted, as well as a slight increase in the overall impedance, indicating a possible degradation of electrodes during the short-term stability test. However, the performance of this AEMWE remains higher than that of other PGM-free anode-based electrolyzers reported in the literature, evaluated at BoT [94–96].

4. Conclusions

A NiFe-based inorganic–organic complex was synthesized via an optimized one-step electrodeposition process for use as an electrocatalyst for OER in water electrolyzers employing AEMs. Succinic acid was employed as the organic linker, which was deprotonated during the electrodeposition, generating succinate ions that reacted with metal ions in solution, promoting the crystallization of Ni^{2+} and/or Fe^{2+} succinate species.

The resulting NiFe-based complex consisted of microparticles composed of nanosheet arrays, leading to a significant increase in the electrochemically active surface area at the nanoscale. This high surface area was also confirmed by EIS through double-layer capacitance measurements. XPS measurements further confirmed the formation of highly active $NiFe_2O_4$ species after electrochemical cycling. The best-performing electrode exhibited an onset potential, η_{onset}, of 240 mV, i.e. 80 mV lower than that of the Fe-only electrode, and an overpotential at 10 mA cm^{-2}, η_{10}, of 306 mV, outperforming other PGM-free OER electrocatalysts reported in the literature, having a total catalyst layer mass loading lower than 1 mg cm^{-2}.

The OER mechanism was studied using DFT calculations, indicating that FeO-(001) surface is more stable than NiO-(001) one. Considering Gibbs free energy, the reaction path predicts the formation of OH* species, followed by an oxidation step leading to OH*OH*. The latter is the rate-determining step, reporting the largest thermodynamic barrier, equal to 0.53 eV, close to the activation energy estimated by using NiFe-based electrode for recording polarization curves at different operating

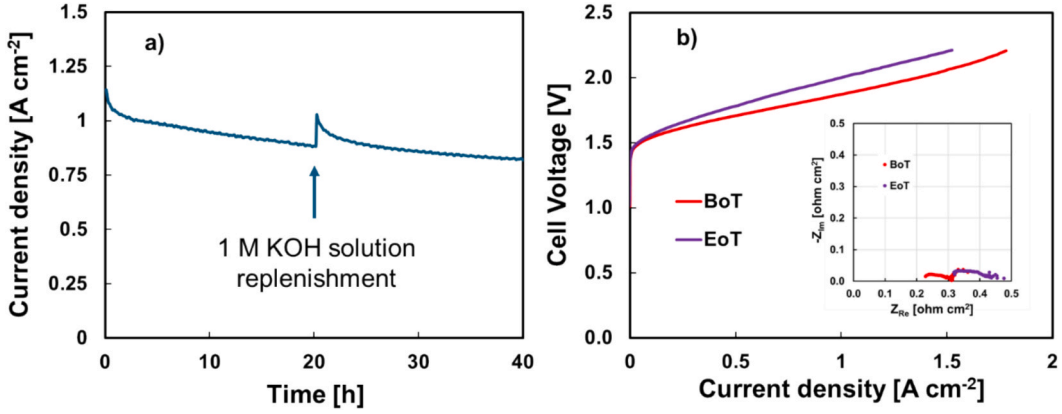

Fig. 12. a) Chronoamperometric durability test carried out at 2 V at 60 °C employing NiFeSuc-15 electrode as anode in an AEMWE. b) LSVs recorded before (BoT) and after (EoT) the durability test at 60 °C. Inset: EIS spectra in Nyquist representation recorded at 2 V before (BoT) and after (EoT) the durability test using the same experimental setup.

temperatures. Then, based on DFT calculations, a comparison between experimental and simulated polarization curves was done, reporting excellent agreement.

Finally, the NiFe-based electrode was integrated as the anode in a single-cell AEM water electrolyzer (AEMWE), demonstrating excellent performance: a current density of 1.86 A cm^{-2} at 60 °C under 2.2 V, with 40 h of stable operation and minimal degradation. This work presents a promising strategy for the development of PGM-free electrocatalysts, contributing to the advancement and practical implementation of AEMWE technology.

CRediT authorship contribution statement

Andrea Zaffora: Writing – review & editing, Writing – original draft, Visualization, Supervision, Methodology, Formal analysis, Conceptualization. **Valentina Maria Volanti:** Writing – original draft, Investigation, Formal analysis, Data curation. **Leonardo Iannucci:** Writing – review & editing, Supervision, Methodology. **Sabrina Grassini:** Writing – review & editing, Supervision, Resources, Methodology. **Ilia Valov:** Writing – review & editing, Supervision, Resources, Methodology. **Clara Saetta:** Writing – original draft, Software, Data curation. **Giovanni Di Liberto:** Writing – review & editing, Supervision, Software, Methodology, Conceptualization. **Erminia Mosca:** Investigation, Data curation. **Irene Gatto:** Writing – review & editing, Supervision, Methodology. **Vincenzo Baglio:** Writing – review & editing, Supervision, Resources, Methodology, Conceptualization. **Monica Santamaria:** Writing – review & editing, Visualization, Supervision, Resources, Project administration, Methodology, Conceptualization.

Declaration of competing interest

The authors declare that they have no known competing financial interests or personal relationships that could have appeared to influence the work reported in this paper.

Acknowledgements

AZ and MS acknowledge the National Recovery and Resilience Plan (PNRR), Mission 2 “Green Revolution and Ecological Transition”, Component 2 “Renewable Energy, Hydrogen, Network and Sustainable Mobility”, Investment 3.5 “Hydrogen Research and Development”, European Union– Next Generation EU Italian Ministry of Environment and Energy Security (MASE), project “AMBITION”. Advanced Technologies Network (ATeN) Center (University of Palermo) is acknowledged for XPS measurements. GDL and CS thank the Italian Supercomputing Center (CINECA) for the availability of computational power via ISCRA B and C projects.

Appendix A. Supplementary data

Supplementary data to this article can be found online at https://doi.org/10.1016/j.fuel.2025.137329.

Data availability

Data will be made available on request.

References

[1] Barbir F. Transition to renewable energy systems with hydrogen as an energy carrier. Energy 2009;34:308–12. https://doi.org/10.1016/J.ENERGY.2008.07.007.
[2] Osman AI, Mehta N, Elgarahy AM, Hefny M, Al-Hinai A, Al-Muhtaseb AH, Rooney DW. Hydrogen production, storage, utilisation and environmental impacts: a review. Environ. Chem. Lett. 2021;20:153–88. https://doi.org/10.1007/S10311-021-01322-8.
[3] Reda B, Elzamar AA, AlFazzani S, Ezzat SM. Green hydrogen as a source of renewable energy: a step towards sustainability, an overview. Environ Dev Sustain 2024:1–21. https://doi.org/10.1007/S10668-024-04892-Z/FIGURES/3.
[4] International Renewable Energy Agency (IRENA), Green Hydrogen Cost Reduction: Scaling up Electrolysers to Meet the 1.5°C Climate Goal, Abu Dhabi, 2020.
[5] Aricò AS, Siracusano S, Briguglio N, Baglio V, Di Blasi A, Antonucci V. Polymer electrolyte membrane water electrolysis: status of technologies and potential applications in combination with renewable power sources. J Appl Electrochem 2013;43:107–18. https://doi.org/10.1007/S10800-012-0490-5/FIGURES/9.
[6] Santoro C, Lavacchi A, Mustarelli P, Di Noto V, Elbaz L, Dekel DR, et al. What is next in Anion-exchange membrane water electrolyzers? Bottlenecks, Benefits, and Future, ChemSusChem 2022;15:e202200027.
[7] Chatenet M, Pollet BG, Dekel DR, Dionigi F, Deseure J, Millet P, et al. Water electrolysis: from textbook knowledge to the latest scientific strategies and industrial developments. Chem Soc Rev 2022;51:4583–762. https://doi.org/10.1039/d0cs01079k.
[8] X. Xie, L. Du, L. Yan, S. Park, Y. Qiu, J. Sokolowski, W. Wang, Y. Shao, Oxygen Evolution Reaction in Alkaline Environment: Material Challenges and Solutions, Adv Funct Mater 32 (2022) 2110036. Doi: 10.1002/ADFM.202110036;JOURNAL:JOURNAL:10990712;PAGE:STRING:ARTICLE/CHAPTER.
[9] McCrory CCL, Jung S, Peters JC, Jaramillo TF. Benchmarking heterogeneous electrocatalysts for the oxygen evolution reaction. J Am Chem Soc 2013;135:16977–87. https://doi.org/10.1021/ja407115p.
[10] Wang M, Wang Z, Li Z, Jian J, Han Q, Chang L. Low-cost Pt–Cu3P/Cu3(PO4)2with outstanding Water Splitting activity in both Basic Solutions and Seawater. ACS Appl Mater Interfaces 2025;17:49556–63. https://doi.org/10.1021/acsami.5c11379.
[11] Sun H, Yan Z, Liu F, Xu W, Cheng F, Chen J. Self-supported transition-metal-based electrocatalysts for hydrogen and oxygen evolution. Adv Mater 2020;32:1806326. https://doi.org/10.1002/ADMA.201806326.
[12] Zhou D, Li P, Xu W, Jawaid S, Mohammed-Ibrahim J, Liu W, et al. Recent advances in non-precious metal-based electrodes for alkaline water electrolysis. ChemNanoMat 2020;6:336–55. https://doi.org/10.1002/cnma.202000010.
[13] Caprì A, Gatto I, Lo Vecchio C, Trocino S, Carbone A, Baglio V. Anion exchange membrane water electrolysis based on nickel ferrite catalysts. ChemElectroChem 2023;10:e202201056. https://doi.org/10.1002/CELC.202201056.
[14] Feng Z, Wang P, Cheng Y, Mo Y, Luo X, Liu P, et al. Recent progress on NiFe2O4 spinels as electrocatalysts for the oxygen evolution reaction. J Electroanal Chem 2023;946:117703. https://doi.org/10.1016/J.JELECHEM.2023.117703.
[15] Mirizzi L, Muhyuddin M, Lo Vecchio C, Mosca E, Baglio V, Gatto I, et al. Amorphous nanostructured Ni–Fe oxide as a notably active and low-cost oxygen evolution reaction electrocatalyst for anion exchange membrane water electrolysis. Ind Chem Mater 2025;3:485–97. https://doi.org/10.1039/d5im00008d.
[16] Chen J, Li T, Shen G, Song Z, Zhong S, Yang Y, et al. Synergistic enhancement of oxygen evolution reaction via NiFe2O4-doped hexagonal nickel hydroxide nanosheets for efficient water electrolysis. Fuel 2025;400. https://doi.org/10.1016/j.fuel.2025.135730.
[17] Zhang Y, Yang Y, Lu B, Zhang RR, Zhou F, Sun D, et al. Bimetallic chloride in situ etching of NiFe alloy substrate to synthesize porous coral structure catalyst for efficient oxygen evolution reaction. Fuel 2025;402. https://doi.org/10.1016/j.fuel.2025.135909.
[18] Jian J, Zhang Y, Wang Z, Zheng X, Nie P, Yang W, et al. One-step synthesized iron foam-based NiFe2O4 applied for self-powered water splitting hydrogen production. J Mater Chem A Mater 2025;13:1102–8. https://doi.org/10.1039/D4TA07904C.
[19] Zheng X, Wang Z, Zeng D, Qiao Y, Li Z, Jian J, et al. NiFe2O4 nanoflowers with Mo doping for self-powered hydrogen production at large current density. J Mater Chem C Mater 2025;13:9099–105. https://doi.org/10.1039/D5TC00624D.
[20] Biradha K, Goswami A, Moi R. Coordination polymers as heterogeneous catalysts in hydrogen evolution and oxygen evolution reactions. Chem Commun 2020;56:10824–42. https://doi.org/10.1039/D0CC04236F.
[21] Zhou Y, Abazari R, Chen J, Tahir M, Kumar A, Ikreedeegh RR, et al. Bimetallic metal–organic frameworks and MOF-derived composites: recent progress on electro- and photoelectrocatalytic applications. Coord Chem Rev 2022;451:214264. https://doi.org/10.1016/J.CCR.2021.214264.
[22] Munawar T, Bashir A, Sardar S, Rafaqat M, Changqing G, Ismail MA, et al. Metal-organic framework-derived defect-enriched bimetallic cerium/manganese oxide nanocomposite with carbon for boosted water electrolysis and supercapacitor applications. Fuel 2026;403. https://doi.org/10.1016/j.fuel.2025.136103.
[23] Sönmez T. Electrochemical performance and kinetics of Mn, Ni, Fe, and Co-loaded covalent triazine frameworks for oxygen evolution reaction in alkaline media. Fuel 2026;403. https://doi.org/10.1016/j.fuel.2025.136106.
[24] Jian J, Wang Z, Qiao Y, Gao S, Wang M, Chang L, et al. NiCoP@CoNi-LDH/SSM as a multifunctional catalyst for high-efficiency water splitting and ultra-long-life rechargeable zinc-air batteries. Green Chem 2024;26:6713–22. https://doi.org/10.1039/D4GC01546K.
[25] Wang Z, Qiao Y, Xue X, Wang M, Nie P, Liu Y, et al. Cobalt carbide-nickel carbide nanosheets supported on CoNi basic carbonates/stainless steel mesh as a trifunctional catalyst for water splitting and Zn-air batteries. ACS Appl Nano Mater 2024;7:27620–7. https://doi.org/10.1021/acsanm.4c05631.
[26] Jian J, Wang Z, Qiao Y, Wang M, Nie P, Chang L. Stainless steel mesh based CoNiSe4/CoNi-layered-double-hydroxides for efficient water-splitting and durable Zn-air battery. J Power Sources 2025;629. https://doi.org/10.1016/j.jpowsour.2024.235994.
[27] Volanti VM, Zaffora A, Iannucci L, Grassini S, Inico E, Saetta C, et al. Design of Ni-coordinated MOF on stainless steel via electrodeposition as efficient and stable

oxygen evolution electrode for alkaline water electrolysis. Electrochim Acta 2025; 511:145416. https://doi.org/10.1016/J.ELECTACTA.2024.145416.
[28] Campagnol N, Van Assche TRC, Li M, Stappers L, Dinca M, Denayer JFM, et al. On the electrochemical deposition of metal-organic frameworks. J Mater Chem A Mater 2016;4:3914–25. https://doi.org/10.1039/c5ta10782b.
[29] Wang CP, Lin YX, Cui L, Zhu J, Bu XH. 2D Metal–organic frameworks as competent electrocatalysts for water splitting. Small 2023;19. https://doi.org/10.1002/smll.202207342.
[30] C. Yang, H. Ma, R. Yuan, K. Wang, K. Liu, Y. Long, F. Xu, L. Li, H. Zhang, Y. Zhang, X. Li, H. Wu, Roll-to-roll prelithiation of lithium-ion battery anodes by transfer printing, Nat Energy 8 (2023) 703–713. Doi: 10.1038/S41560-023-01272-1; SUBJMETA=1032,299,301,639,891,930;KWRD=BATTERIES,DESIGN.
[31] A. Carbone, R. Pedicini, I. Gatto, A. Saccà, A. Patti, G. Bella, M. Cordaro, Development of Polymeric Membranes Based on Quaternized Polysulfones for AMFC Applications, Polymers 2020, Vol. 12, Page 283 12 (2020) 283. Doi: 10.3390/POLYM12020283.
[32] Hafner J. Ab-initio simulations of materials using VASP: density-functional theory and beyond. J Comput Chem 2008;29:2044–78. https://doi.org/10.1002/jcc.21057.
[33] J.P. Perdew, K. Burke, M. Ernzerhof, Generalized Gradient Approximation Made Simple, 1996.
[34] G. Kresse, D. Joubert, From ultrasoft pseudopotentials to the projector augmented-wave method, n.d.
[35] Verma P, Truhlar DG. Does DFT+U mimic hybrid density functionals? Theor Chem Acc 2016;135. https://doi.org/10.1007/s00214-016-1927-4.
[36] Ö.N. Avcl, L. Sementa, A. Fortunelli, Mechanisms of the Oxygen Evolution Reaction on NiFe2O4and CoFe2O4Inverse-Spinel Oxides, ACS Catal 12 (2022) 9058–9073. Doi: 10.1021/ACSCATAL.2C01534/ASSET/IMAGES/LARGE/CS2C01534_0013.JPEG.
[37] Barlocco I, Cipriano LA, Di Liberto G, Pacchioni G. Does the oxygen evolution reaction follow the classical oH*, O*, oOH* path on single atom catalysts? J Catal 2023;417:351–9. https://doi.org/10.1016/J.JCAT.2022.12.014.
[38] Nørskov JK, Bligaard T, Rossmeisl J, Christensen CH. Towards the computational design of solid catalysts. Nat Chem 2009;1:37–46. https://doi.org/10.1038/NCHEM.121;KWRD=CHEMISTRY.
[39] Li M, Dincă M. Selective formation of biphasic thin films of metal-organic frameworks by potential-controlled cathodic electrodeposition. Chem Sci 2014;5:107–11. https://doi.org/10.1039/c3sc51815a.
[40] Wang Z, Liu H, Wang S, Rao Z, Yang Y. A luminescent Terbium-Succinate MOF thin film fabricated by electrodeposition for sensing of Cu2+ in aqueous environment. Sens Actuators B Chem 2015;220:779–87. https://doi.org/10.1016/j.snb.2015.05.129.
[41] Zhang X, Wan K, Subramanian P, Xu M, Luo J, Fransaer J. Electrochemical deposition of metal-organic framework films and their applications. J Mater Chem A Mater 2020;8:7569–87. https://doi.org/10.1039/d0ta00406e.
[42] Patnaik SG, Vanheusden G, Saleh AA, Vereecken PM. Electrochemically induced deposition (ECiD): a versatile method that greatly extends the portfolio of surface coatings and materials fabricated by electrochemical deposition. Electrochem Soc Interface 2024;33:61–6. https://doi.org/10.1149/2.F11242IF/XML.
[43] Nageswaran VMVG. Review—direct electrochemical synthesis of metal organic frameworks. J Electrochem Soc 2020;167:155527. https://doi.org/10.1149/1945-7111/abc6c6.
[44] A. Zaffora, B. Megna, B. Seminara, F. Di Franco, M. Santamaria, Ni,Fe,Co-LDH Coated Porous Transport Layers for Zero-Gap Alkaline Water Electrolyzers, Nanomaterials 2024, Vol. 14, Page 407 14 (2024) 407. Doi: 10.3390/NANO14050407.
[45] Gao X, Chen D, Qi J, Li F, Song Y, Zhang W, et al. NiFe oxalate nanomesh array with homogenous doping of fe for electrocatalytic water oxidation. Small 2019;15:1904579. https://doi.org/10.1002/SMLL.201904579;SUBPAGE:STRING:FULL.
[46] D.A. Nurani, B.C.B. Butar, Y.K. Krisnandi, Synthesis and characterization of metal organic framework using succinic acid ligand with cobalt and iron metals as methylene blue dye adsorbent, in: IOP Conf Ser Mater Sci Eng, IOP Publishing Ltd, 2020. Doi: 10.1088/1757-899X/902/1/012055.
[47] Li CF, Xie LJ, Zhao JW, Gu LF, Tang HB, Zheng L, et al. Interfacial Fe−O−Ni−O−Fe bonding regulates the active Ni sites of Ni-MOFs via iron doping and decorating with FeOOH for super-efficient oxygen evolution. Angew Chem Int Ed 2022;61. https://doi.org/10.1002/ANIE.202116934;PAGE:STRING:ARTICLE/CHAPTER.
[48] Yilmaz VT, Demir S, Andac O, Harrison W. Mixed-ligand metal succinate complexes with 1,10-phenanthroline and ethylenediamine: synthesis, characterization, spectroscopic and thermal studies. Crystal structure of succinatocobalt(II) complex with phenanthroline. J Coord Chem 2002;55:863–72.
[49] Bieńko D, Malik-Gajewska M, Walencik P, Kaj M, Zierkiewicz W, Murtaza G, et al. IR and Raman spectroscopic analysis, DFT modeling, and magnetic properties of a nickel(II) complex, [Ni(succ)(H2O)4]n. J Coord Chem 2019;72:2215–32. https://doi.org/10.1080/00958972.2019.1650351.
[50] Krishnan S, Raj CJ, Robert R, Ramanand A, Jerome Das S. Growth and characterization of succinic acid single crystals. Cryst Res Technol 2007;42:1087–90. https://doi.org/10.1002/crat.200710981.
[51] Biesinger MC, Payne BP, Lau LWM, Gerson A, Smart RSC. X-ray photoelectron spectroscopic chemical state quantification of mixed nickel metal, oxide and hydroxide systems. Surf Interface Anal 2009;41:324–32.
[52] Biesinger MC, Lau LWM, Gerson AR, Smart RSC. Resolving surface chemical states in XPS analysis of first row transition metals, oxides and hydroxides: Sc, Ti, V, Cu and Zn. Appl Surf Sci 2010;257:887–98. https://doi.org/10.1016/J.APSUSC.2010.07.086.
[53] Yamashita T, Hayes P. Analysis of XPS spectra of Fe2+ and Fe3+ ions in oxide materials. Appl Surf Sci 2008;254:2441–9. https://doi.org/10.1016/J.APSUSC.2007.09.063.
[54] Taheri P, Hauffman T, Mol JMC, Flores JR, Hannour F, De Wit JHW, et al. Molecular interactions of electroadsorbed carboxylic acid and succinic anhydride monomers on zinc surfaces. J Phys Chem C 2011;115:17054–67.
[55] Wang X, Du D, Xu H, Yan Y, Wen X, Ren L, et al. NiMn-based metal-organic framework with optimized eg orbital occupancy as efficient bifunctional electrocatalyst for lithium-oxygen batteries. Chem Eng J 2023;452:139524. https://doi.org/10.1016/J.CEJ.2022.139524.
[56] Li Z, Yao Y, Sun S, Liang J, Hong S, Zhang H, et al. Carbon oxyanion self-transformation on NiFe oxalates enables long-term ampere-level current density seawater oxidation. Angew Chem Int Ed 2024;63:e202316522. https://doi.org/10.1002/ANIE.202316522.
[57] Hirschorn B, Orazem ME, Tribollet B, Vivier V, Frateur I, Musiani M. Determination of effective capacitance and film thickness from constant-phase-element parameters. Electrochim Acta 2010;55:6218–27. https://doi.org/10.1016/j.electacta.2009.10.065.
[58] Zaffora A, Di Franco F, Pupillo D, Seminara B, Tranchida G, Santamaria M. Highly active and stable NiCuMo electrocatalyst supported on 304 stainless steel porous transport layer for hydrogen evolution in alkaline water electrolyzer. Adv Sustain Syst 2023;7. https://doi.org/10.1002/adsu.202200486.
[59] Zhao J, Zhang J, Li Z, Bu X. Recent progress on NiFe-based electrocatalysts for the oxygen evolution reaction. Small 2020;16. https://doi.org/10.1002/smll.202003916.
[60] L. Magnier, G. Cossard, V. Martin, C. Pascal, V. Roche, E. Sibert, I. Shchedrina, R. Bousquet, V. Parry, M. Chatenet, Fe–Ni-based alloys as highly active and low-cost oxygen evolution reaction catalyst in alkaline media, Nature Materials 2024 23:2 23 (2024) 252–261. Doi: 10.1038/s41563-023-01744-5.
[61] Zhu Y, Cai Z, Wei Q, Chen R, Guo F, Jiang Y, et al. Asymmetric electron transport-induced formation of high-valent IrOx in NiFeOOH heterostructure for efficient water oxidation. Adv Funct Mater 2025. https://doi.org/10.1002/adfm.202503692.
[62] van der Heijden O, Park S, Eggebeen JJJ, Koper MTM. Non-kinetic effects convolute activity and tafel analysis for the alkaline oxygen evolution reaction on NiFeOOH electrocatalysts. Angew Chem Int Ed 2023;62. https://doi.org/10.1002/ANIE.202216477.
[63] van der Heijden O, Park S, Vos RE, Eggebeen JJJ, Koper MTM. Tafel slope plot as a tool to analyze electrocatalytic reactions. ACS Energy Lett 2024;9:1871–9. https://doi.org/10.1021/ACSENERGYLETT.4C00266/ASSET/IMAGES/LARGE/NZ4C00266_0004.JPEG.
[64] Tang L, Li M, Zhang al Y, Zhou J-P, Lv L, Liu Q, Jiang Z, Chen L, Shi N, Sartale SD, Lokhande CD, Giersig M, Ganesan V. Novel electrochemical process for the deposition of nanocrystallineNiFe2O4 thin films. J Phys Condens Matter 2004;16:773. https://doi.org/10.1088/0953-8984/16/6/008.
[65] Hua M, Xu L, Cui F, Lian J, Huang Y, Bao J, et al. Hexamethylenetetramine-assisted hydrothermal synthesis of octahedral nickel ferrite oxide nanocrystallines with excellent supercapacitive performance. J Mater Sci 2018;53:7621–36. https://doi.org/10.1007/S10853-018-2052-7/TABLES/3.
[66] Liu Z, Li Y, Ding Y, Huang W, Hao Y, Wang T, et al. Electrochemically engineered fabricated NiOOH/NiO nanospheres with oxygen vacancies for enhanced oxygen evolution reaction. Fuel 2026;404. https://doi.org/10.1016/j.fuel.2025.136249.
[67] Corrigan DA. The catalysis of the oxygen evolution reaction by iron impurities in thin film nickel oxide electrodes. J Electrochem Soc 1987;134:377–84. https://doi.org/10.1149/1.2100463/PDF.
[68] Trotochaud L, Young SL, Ranney JK, Boettcher SW. Nickel–iron oxyhydroxide oxygen-evolution electrocatalysts: the role of intentional and incidental iron incorporation. J Am Chem Soc 2014;136:6744–53. https://doi.org/10.1021/JA502379C.
[69] Friebel D, Louie MW, Bajdich M, Sanwald KE, Cai Y, Wise AM, et al. Identification of highly active Fe Sites in (Ni,Fe)OOH for electrocatalytic water splitting. J Am Chem Soc 2015;137:1305–13. https://doi.org/10.1021/JA511559D.
[70] Zhou Y, Wang Z, Cui M, Wu H, Liu Y, Ou Q, et al. NiFe-Based electrocatalysts for alkaline oxygen evolution: challenges, strategies, and advances toward industrial-scale deployment. Adv Funct Mater 2024;34. https://doi.org/10.1002/adfm.202410618.
[71] Song W, Xia C, Zaman S, Chen S, Xiao C. Advances in stability of NiFe-based anodes toward oxygen evolution reaction for alkaline water electrolysis. Small 2024;20. https://doi.org/10.1002/smll.202406075.
[72] Zhang F, Shi Y, Xue T, Zhang J, Liang Y, Zhang B. In situ electrochemically converting Fe2O3-Ni(OH)2 to NiFe2O4-NiOOH: a highly efficient electrocatalyst towards water oxidation. Sci China Mater 2017;60:324–34. https://doi.org/10.1007/s40843-017-9017-6.
[73] Dalai N, Mohanty B, Mitra A, Jena B. Highly active ternary nickel–iron oxide as bifunctional catalyst for electrochemical water splitting. ChemistrySelect 2019;4:7791–6. https://doi.org/10.1002/slct.201901465.
[74] Xiang W, Hernandez S, Hosseini P, Bai F, Hagemann U, Heidelmann M, et al. Unveiling surface species formed on Ni-Fe spinel oxides during the oxygen evolution reaction at the atomic scale. Adv Sci 2025;12. https://doi.org/10.1002/advs.202501967.
[75] Shinagawa T, Takanabe K. New insight into the hydrogen evolution reaction under buffered near-neutral pH conditions: enthalpy and entropy of activation. J Phys Chem C 2016;120:24187–96. https://doi.org/10.1021/ACS.JPCC.6B07954/ASSET/IMAGES/LARGE/JP-2016-07954F_0006.JPEG.
[76] Nurlaela E, Shinagawa T, Qureshi M, Dhawale DS, Takanabe K. Temperature dependence of electrocatalytic and photocatalytic oxygen evolution reaction rates

using NiFe oxide. ACS Catal 2016;6:1713–22. https://doi.org/10.1021/ACSCATAL.5B02804/ASSET/IMAGES/CS-2015-02804P_M011.GIF.
[77] Suermann M, Schmidt TJ, Büchi FN. Comparing the kinetic activation energy of the oxygen evolution and reduction reactions. Electrochim Acta 2018;281:466–71. https://doi.org/10.1016/J.ELECTACTA.2018.05.150.
[78] Li Y, Zhang T, Ma J, Deng X, Gu J, Yang F, et al. Study the effect of lye flow rate, temperature, system pressure and different current density on energy consumption in catalyst test and 500W commercial alkaline water electrolysis. Mater Today Phys 2022;22:100606. https://doi.org/10.1016/J.MTPHYS.2022.100606.
[79] F. Rocha, C. Georgiadis, K. Van Droogenbroek, R. Delmelle, X. Pinon, G. Pyka, G. Kerckhofs, F. Egert, F. Razmjooei, S.A. Ansar, S. Mitsushima, J. Proost, Proton exchange membrane-like alkaline water electrolysis using flow-engineered three-dimensional electrodes, Nature Communications 2024 15:1 15 (2024) 1–13. Doi: 10.1038/s41467-024-51704-z.
[80] Avcı ÖN, Sementa L, Fortunelli A. Atomistic modeling of spinel oxide particle shapes and reshaping under OER conditions. Physchem 2024;4:43–60. https://doi.org/10.3390/PHYSCHEM4010004/S1.
[81] Shi X, Li YF, Bernasek SL, Selloni A. Structure of the NiFe2O4(001) surface in contact with gaseous O2 and water vapor. Surf Sci 2015;640:73–9. https://doi.org/10.1016/J.SUSC.2015.03.012.
[82] Shi X, Bernasek SL, Selloni A. Mechanism and activity of CO oxidation on (001) and (110) surfaces of spinel Co3O4, NiCo2O4 and NiFe2O4: a DFT + U study. Surf Sci 2018;677:278–83. https://doi.org/10.1016/J.SUSC.2018.08.002.
[83] Di Liberto G, Pacchioni G. Modeling single-atom catalysis. Adv Mater 2023;35:2307150. https://doi.org/10.1002/ADMA.202307150;REQUESTEDJOURNAL:JOURNAL:15214095;WGROUP:STRING:PUBLICATION.
[84] Razzaq S, Exner KS. Materials screening by the descriptor Gmax(η): the free-energy span model in electrocatalysis. ACS Catal 2023;13:1740–58. https://doi.org/10.1021/ACSCATAL.2C03997/ASSET/IMAGES/LARGE/CS2C03997_0018.JPEG.
[85] Caprì A, Martínez-Lázaro A, Béjar J, Gatto I, Álvarez-Contreras L, Gurrola MP, et al. Three-dimensionally ordered macroporous trimetallic spinel for anion exchange membrane water electrolysis. Electrochim Acta 2023;463:142851. https://doi.org/10.1016/J.ELECTACTA.2023.142851.
[86] Martinez-Lazaro A, Caprì A, Gatto I, Ledesma-García J, Rey-Raap N, Arenillas A, et al. NiFe2O4 hierarchical nanoparticles as electrocatalyst for anion exchange membrane water electrolysis. J Power Sources 2023;556:232417. https://doi.org/10.1016/J.JPOWSOUR.2022.232417.
[87] Simari C, Caprì A, Ur Rehman MH, Enotiadis A, Gatto I, Baglio V, et al. Composite anion exchange membranes based on polysulfone and silica nanoscale ionic materials for water electrolyzers. Electrochim Acta 2023;462:142788. https://doi.org/10.1016/J.ELECTACTA.2023.142788.
[88] Carboni N, Mazzapioda L, Caprì A, Gatto I, Carbone A, Baglio V, et al. Composite anion exchange membranes based on graphene oxide for water electrolyzer applications. Electrochim Acta 2024;486:144090. https://doi.org/10.1016/J.ELECTACTA.2024.144090.
[89] Montalto M, da Freitas WS, Mastronardo E, Ficca VCA, Placidi E, Baglio V, Mosca E, Lo Vecchio C, Gatto I, Mecheri B, D'Epifanio A. Spinel-type high-entropy oxides for enhanced oxygen evolution reaction activity in anion exchange membrane water electrolyzers. Chem Eng J 2025;507:160641. https://doi.org/10.1016/J.CEJ.2025.160641.
[90] Osorio J, Quiroz SG, Cartagena S, Calderón JA. Realistic electrolyzer temperature and pressure conditions evaluation of NiFeP/Zn-coated electrodes for alkaline water splitting. Fuel 2026;404. https://doi.org/10.1016/j.fuel.2025.136339.
[91] S. Siracusano, S. Trocino, N. Briguglio, V. Baglio, A.S. Aricò, Electrochemical Impedance Spectroscopy as a Diagnostic Tool in Polymer Electrolyte Membrane Electrolysis, Materials 2018, Vol. 11, Page 1368 11 (2018) 1368. Doi: 10.3390/MA11081368.
[92] Ahmed KW, Habibpour S, Chen Z, Fowler M. Investigation of NiCoOx catalysts for anion exchange membrane water electrolysis: performance, durability, and efficiency analysis. J Energy Storage 2024;79:110149. https://doi.org/10.1016/J.EST.2023.110149.
[93] Ranz M, Grabner B, Schweighofer B, Wegleiter H, Trattner A. Dynamics of anion exchange membrane electrolysis: unravelling loss mechanisms with electrochemical impedance spectroscopy, reference electrodes and distribution of relaxation times. J Power Sources 2024;605:234455. https://doi.org/10.1016/J.JPOWSOUR.2024.234455.
[94] Park JE, Kim MJ, Lim MS, Kang SY, Kim JK, Oh SH, et al. Graphitic carbon nitride-carbon nanofiber as oxygen catalyst in anion-exchange membrane water electrolyzer and rechargeable metal–air cells. Appl Catal B 2018;237:140–8. https://doi.org/10.1016/J.APCATB.2018.05.073.
[95] Caielli T, Ferrari AR, Bonizzoni S, Sediva E, Caprì A, Santoro M, et al. Synthesis, characterization and water electrolyzer cell tests of poly(biphenyl piperidinium) Anion exchange membranes. J Power Sources 2023;557:232532. https://doi.org/10.1016/J.JPOWSOUR.2022.232532.
[96] S. Li, T. Liu, W. Zhang, M. Wang, H. Zhang, C. Qin, L. Zhang, Y. Chen, S. Jiang, D. Liu, X. Liu, H. Wang, Q. Luo, T. Ding, T. Yao, Highly efficient anion exchange membrane water electrolyzers via chromium-doped amorphous electrocatalysts, Nature Communications 2024 15:1 15 (2024) 1–11. Doi: 10.1038/s41467-024-47736-0.